ELSEVIER

Atmospheric Research 59–60 (2001) 295–312

ATMOSPHERIC RESEARCH

www.elsevier.com/locate/atmos

Remote sensing of cloud thickness and liquid water content with Wide-Angle Imaging Lidar

Steven P. Love, Anthony B. Davis *, Cheng Ho, Charles A. Rohde

Space and Remote Sensing Sciences Group, Los Alamos National Laboratory, Los Alamos, NM 87545, USA

Accepted 13 August 2001

Abstract

We describe a new type of lidar instrument, Wide-Angle Imaging Lidar (WAIL), designed to study and directly make use of multiple scattering in clouds. Providing time-resolved imagery over a 60° field of view, the new instrument captures returns at virtually all orders of scattering in a ground-based measurement. We report the first retrievals of cloud properties using this system, from measurements of a moderately opaque altostratus. Following insights from photon diffusion theory, we are able to infer the physical thickness and optical depth of the cloud layer, and, from there, obtain an estimate of the volume-averaged liquid water content. Performance of the new instrument is discussed and it is compared with other active techniques in cloud remote sensing.

Keywords: Lidar; Multiple scattering; Photon diffusion; Boundary-layer clouds; Stratiform clouds; Remote sensing; Instrumentation

1. Introduction

For remote sensing of cloud properties, traditional ‘‘on-beam’’ lidar, which collects returns from only a very narrow field-of-view (FOV) centered on the transmitted laser beam, yields only a small fraction of the information potentially available. For the optically thick clouds typical of the boundary layer, conventional lidar is typically limited to providing the range to the first interface (i.e., ceilometry from ground; cloud-top range from airborne platforms), though with some extra effort, information about the

* Corresponding author.
E-mail address: adavis@lanl.gov (A.B. Davis).

0169-8095/01/$ - see front matter
PII: S0169-8095(01)00121-1

water phase in the first layers can also be inferred by using depolarization (Sassen, 1994) or multiple-FOV measurements (Bissonnette, 1995). This limitation is largely an artificial one, however. The key to the work described here is the recognition that, at most visible and near-IR wavelengths, lidar photons are not absorbed but merely scattered out of the beam. Much additional information exists in these multiply scattered photons exiting the cloud far from the input beam. Such photons have typically undergone many scattering events, and have thoroughly sampled the cloud's internal structure before they eventually reemerge, sometimes as much as a kilometer from the input beam. Here we describe a new type of lidar instrument, Wide-Angle Imaging Lidar (WAIL), which aims specifically at measuring these large-displacement returns. With a field-of-view of approximately 1 rad, our ground-based instrument provides time-resolved 2D imaging of the returning light, or in essence, "movies" of the light propagation. Mathematically speaking, by measuring the complete spatial and temporal profiles of the returning light, WAIL in effect measures the Green functions (GFs), or radiative impulse response functions, of the cloud, since a pulsed laser is essentially a Dirac δ-function in space and time. The temporal Green function, essentially the time dependence of the spatially integrated return, is directly related to the distribution of photon pathlengths and is of interest in itself.

A key insight, allowing cloud properties to be extracted from WAIL data, was obtained by Davis et al. (1997a, 1999): the extent of the temporal Green function (i.e., its decay time) is dominated by the physical thickness of the cloud, while the lateral extent of spatial Green function (i.e., its root-mean-square diameter), is influenced strongly by cloud optical depth. Thus both the thickness of the cloud and its optical density can be inferred from off-beam lidar. These two cloud properties are of direct interest in a variety of meteorological applications, most notably to clarify the effect of clouds on atmospheric radiative transfer and energy deposition for climate modeling. In addition, once the cloud thickness and optical density are determined, one can infer the liquid water content (LWC), in a volume-averaged manner, via the mean extinction coefficient (i.e., optical depth divided by cloud thickness) together with an educated guess at the effective drop radius. This represents a significant increase in information obtainable from lidar; due to their extreme opacity, the only way to obtain these properties for dense boundary-layer clouds using a conventional lidar is to over- and under-fly the layer using an airborne system (Pelon et al., 2000).

We report here on the status of the emerging technology in WAIL, as implemented for ground-based observations, and the associated retrieval schemes. Davis et al. (in press) give a complementary account of cloud-property retrievals based on lidar data collected in space during the Lidar-In-Space Technology Experiment (LITE). In spite of the standard narrow FOV of the LITE system (3.5 mrad at night), the data is essentially off-beam due to the unusually large (260 km) range of the target cloud, hence a 0.91 km footprint of the detector.

The paper is organized as follows. In the next section, we survey the basic theory of off-beam cloud lidar. Section 3 describes the WAIL system phototype assembled at LANL. In Section 4, we present field data from this instrument and use it to infer cloud properties. In Section 5, we summarize our findings and outline future work.

2. Off-beam cloud lidar theory

Here we present an overview of the theory of off-beam lidar. The key results of greatest interest here are given in Eqs. (9) and (11) below. These results are (a) that the mean pathlength of the returning lidar photons, $\langle\lambda\rangle_R$, is (apart from a small correction) proportional to the cloud physical thickness H, and (b) that the mean-square radius of the diffuse spot, $\langle\rho^2\rangle_R$, is (again, apart from a small correction) proportional to the cloud thickness squared divided by the optical depth, τ.

2.1. Definitions

The schematic in Fig. 1 shows the geometry of off-beam cloud lidar observations. The key quantities are cloud optical depth (τ), physical thickness (H), asymmetry factor of the scattering phase function (g), and range (d_{obs}). We are interested exclusively in the remotely observable radiative transfer GF(obs), that is, for escaping radiation, excited by a δ-function source at the cloud boundary. It will depend parametrically on all of the above cloud quantities as well as two independent variables for space and one for time. The spatial variables can be expressed as Cartesian coordinates (x, y), cylindrical coordinates (ρ, φ), or polar angles (θ_ρ, φ). The temporal variable can be either time elapsed since the pulse impacted the cloud (t), or the "in-cloud" pathlength ($\lambda=ct$), noting that the "out-of-cloud" portion of total pathlength is simply $d_{obs}(1+1/\cos\theta_\rho)$.

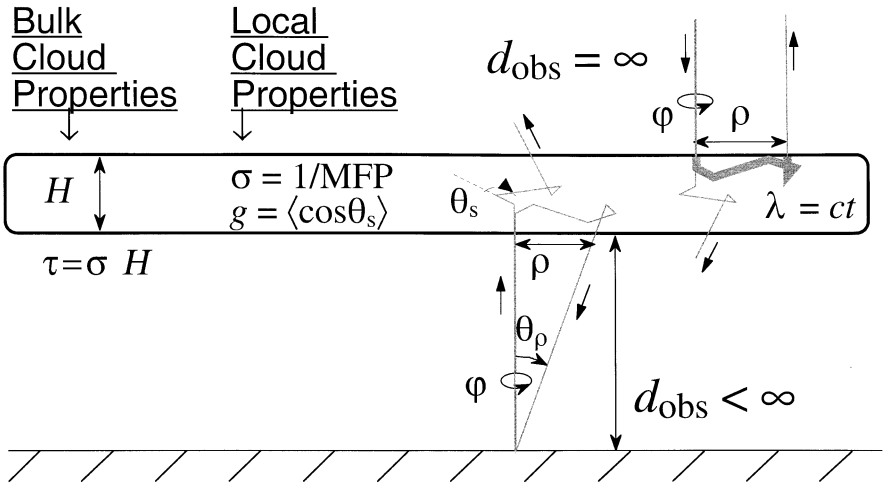

Fig. 1. Geometry of off-beam cloud lidar. From left to right, illustrated meanings for: (1) cloud optical depth τ, physical thickness H, their ratio (extinction σ), and asymmetry factor g (mean cosine of scattering angle ≈ 0.85 for typical droplet populations); (2) independent variables angle (space) θ_ρ and time t, radiance G_{obs} (τ, g, H, d_{obs}; t, θ_ρ, φ) for a ground-based WAIL system and a cloud at finite range d_{obs}; (3) similarly, G_{obs} (τ, g, H, ∞; t, ρ, φ) is measured during a LITE-like mission in space and has been extensively studied elsewhere (Winker, 1997; Miller and Stephens, 1999; Davis et al., in press).

Photon-escape GFs have straightforward interpretations in terms of probability of a photon to escape from the cloud into any direction at position (x, y) and time t, conditional to be either reflected or transmitted: e.g.,

$$G_{\mathrm{R}}(t,x,y)\mathrm{d}x\mathrm{d}y\mathrm{d}t/R = \mathrm{Prob}\{\text{escape during}[t,t+\mathrm{d}t),\ \text{from}\ [x,x+\mathrm{d}x)\otimes[y,y+\mathrm{d}y)\ \text{in reflection}\}, \tag{1}$$

where the normalization constant,

$$R = \int\int\int G_{\mathrm{R}}(t,x,y)\mathrm{d}x\mathrm{d}y\mathrm{d}t, \tag{2}$$

is simply cloud albedo for normal incidence, assuming the integrated pulse energy is unity. This normalized escape GF can be thus treated as a probability density function (PDF) and we can proceed to compute its moments. An analogous GF can be defined for transmission where, by conservation at most lidar wavelengths, we have $T=1-R$. In this paper we are primarily concerned with the reflection geometry; the subscript "R" on various quantities in the discussion that follows indicates that these quantities are calculated for the reflection geometry.

If detailed information about the space/time-dependent bi-directional properties of the cloud's radiative GFs is not available, then we make a standard Lambertian hypothesis:

$$G_{\mathrm{R}}(t,x,y)\mathrm{d}x\mathrm{d}y\mathrm{d}t \approx \pi G_{\mathrm{obs}}(t,\theta_\rho,\varphi)d_{\mathrm{obs}}^2\sin\theta_\rho\mathrm{d}\theta_\rho\mathrm{d}\varphi\mathrm{d}t. \tag{3}$$

The l.h.s. can be computed analytically in diffusion theory while the r.h.s. can be obtained from monostatically collected data (cf. Fig. 1). Using a numerical Monte Carlo (MC) model, Davis and Cahalan (1998) show that biases associated with the Lambertian assumption tend to cancel in the following spatial integrals, hence do not dominate the error budget.

The simplest in-cloud propagation characteristics of a laser pulse are: the mean photon pathlength,

$$\langle\lambda\rangle_{\mathrm{R}} = c\langle t\rangle_{\mathrm{R}} = c\int\int\mathrm{d}x\mathrm{d}y\left[\int tG_{\mathrm{R}}(t,x,y)\mathrm{d}t\right]/R; \tag{4}$$

its 2nd-order moment (used, for instance, in pathlength variance $\langle\lambda^2\rangle_{\mathrm{R}}-\langle\lambda\rangle_{\mathrm{R}}^2$),

$$\langle\lambda^2\rangle_{\mathrm{R}} = c^2\langle t^2\rangle_{\mathrm{R}} = c^2\int\int\mathrm{d}x\mathrm{d}y\left[\int t^2G_{\mathrm{R}}(t,x,y)\mathrm{d}t\right]/R; \tag{5}$$

and root-mean-square (rms) horizontal transport $\langle\rho^2\rangle_{\mathrm{R}}^{1/2}$, where

$$\langle\rho^2\rangle_{\mathrm{R}} = \int\mathrm{d}t\left[\int\int(x^2+y^2)G_{\mathrm{R}}(t,x,y)\mathrm{d}x\mathrm{d}y\right]/R. \tag{6}$$

One can think of $\langle\rho^2\rangle_{\mathrm{R}}^{1/2}$ as the gyration radius of the spot diffuse light excited by the laser in cw mode. A major advantage of using the observables in Eqs. (4)–(6) is that there is no need for absolute calibration to estimate them from observations using Eqs. (1)–(3).

There are of course analogous quantities for transmission (subscript "T") that have been used in other studies: Veitel et al. (1998) and Savigny et al. (1999) for empirical

results, respectively, in the temporal and spatial domains; Davis and Marshak (submitted for publication) for the detailed theory that is, in large part, also germane to reflection.

2.2. Analytical results from diffusion theory

In absence of absorption, only two length scales are required to determine the optical properties of a plane-parallel medium in space/time as well as for constant/uniform illumination:

- the outer scale given by the physical thickness H, and
- the inner scale defined by the photon mean-free-path (MFP), $l=1/\sigma=H/\tau$.

In the diffusion approximation, we are actually more interested in the "transport" MFP

$$l_{\mathrm{t}} = l/(1-g) = 1/[(1-g)\sigma] \tag{7}$$

which, in essence, is the MFP for an effectively isotropic scattering; the rescaling by $(1-g)^{-1}\approx 6.7$ for $g=0.85$ takes care of the propensity for forward (Mie) scattering by the cloud droplets (Deirmendjian, 1969). One final parameter is introduced in diffusion theory to describe boundary conditions: "extrapolation length" which we will denote χl_{t}. Here χ is an O(1) numerical factor that can be used to minimize the approximation error although it is often set to 2/3, following Eddington (1916) prescription, or to $0.7104\cdots$, following asymptotic radiative tranfer theory (Case and Zweifel, 1967).

A spatial-Fourier/temporal-Laplace solution of the non-stationary 3D diffusion equation by Davis et al. (1999) with boundary/initial conditions describing a pulsed point-source leads to:

$$R = \frac{H}{2\chi l_t + H} = \frac{(1-g)\tau}{2\chi + (1-g)\tau} \tag{8}$$

for albedo in Eq. (2);

$$\langle\lambda\rangle_{\mathrm{R}} = 2\chi H[1 + C_{\mathrm{R}\lambda}(1,\varepsilon)] \tag{9}$$

for mean pathlength in Eq. (4); and

$$\langle\lambda^2\rangle_{\mathrm{R}} = \frac{4\chi}{5} H^2(1-g)\tau[1 + C_{\mathrm{R}\lambda}(2,\varepsilon)] \tag{10}$$

for the 2nd moment of pathlength in Eq. (5); and

$$\langle\rho^2\rangle_{\mathrm{R}} = \frac{8\chi}{3}\,\frac{H^2}{(1-g)\tau}\,[1 + C_{\mathrm{R}\rho}(2,\varepsilon)] \tag{11}$$

for the variance in horizontal transport defined in Eq. (6). The radiative quantities in Eqs. (9)–(11) contain pre-asymptotic correction terms given by:

$$C_{\mathrm{R}\lambda}(1,\varepsilon) = C_{\mathrm{R}\rho}(2,\varepsilon) = (\varepsilon/2)(1+3\varepsilon/2)/(1+\varepsilon), \tag{12a}$$

$$C_{\mathrm{R}\lambda}(2,\varepsilon) = (\varepsilon/2)(8+41\varepsilon/2+75\varepsilon^2/4+\varepsilon^3/8)/(1+\varepsilon)^2; \tag{12b}$$

these corrections become small as

$$\varepsilon = 2\chi/(1-g)\tau = 2\chi l_t/H = T/R \tag{13}$$

decreases (τ increases).

We note that, apart from the precise proportionally constants dependent on χ, the leading terms in Eqs. (8)–(10) can be obtained from simple arguments based on the scaling/fractal properties of the random walks (Mandelbrot, 1982) executed by the lidar photons in the finite slab that defines the cloud. See Davis et al. (1997a) for R, $\langle\lambda\rangle_R$, and $\langle\rho^2\rangle_R$, and Davis (1999) for $\langle\lambda^2\rangle_R$. For instance, the well-known fact that the (implicitly mean) order-of-scattering in reflected light goes as τ translates here to $\langle\lambda\rangle_R \propto H$, as can be seen in Eq. (9).

2.3. Comparison with Monte Carlo results

Going from bottom to top, Fig. 2 shows $T = 1-R$, $\langle\rho^2\rangle_R^{1/2}$, $\langle\lambda\rangle_R$, and $\langle\lambda^2\rangle_R^{1/2}$ from Eqs. (8), (9), (10), (11), (12a,b) and (13) with $H = 1$ for simplicity and $\chi = 0.57$ to best reproduce the numerical result from straightforward MC simulations (symbols). Agree-

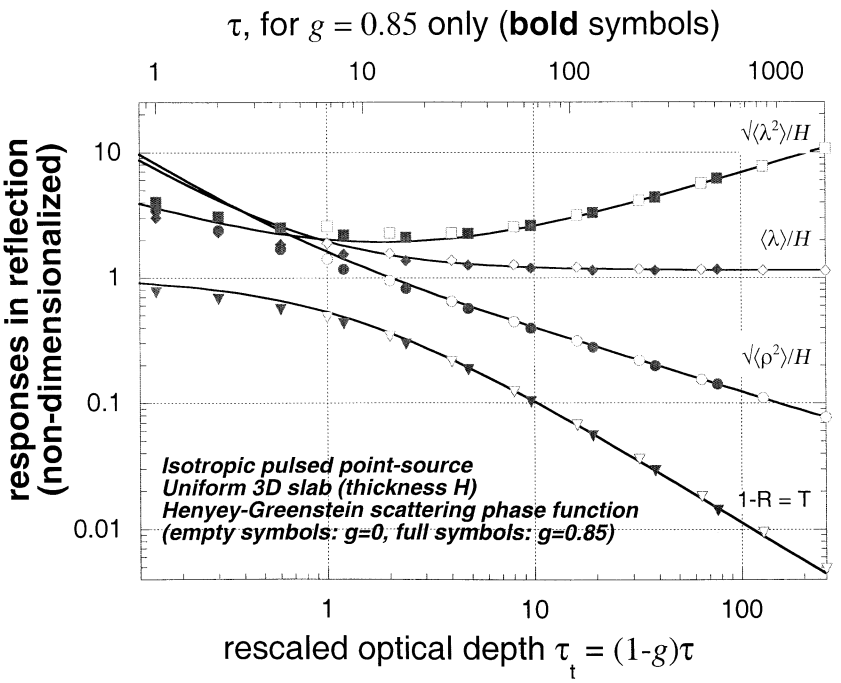

Fig. 2. Analytical and numerical results for off-beam cloud lidar observables. From bottom to top at right, we plotted $T = 1-R$, $\langle\rho^2\rangle_R^{1/2}/H$, $\langle\lambda\rangle_R/H$, and $\langle\lambda^2\rangle_R^{1/2}/H$, from Eqs. (8), (9), (10), (11), (12a,b) and (13) with $\chi = 0.57$. Monte Carlo results are plotted for phase functions both isotropic and forward-scattering, where a Henyey and Greenstein (1941) model with $g = 0.85$ was used. We note the collapse of the numerical results for the most part onto their analytical counterparts, when plotted against $(1-g)\tau = H/l_t$.

ment is excellent in the asymptotic regime, $(1-g)\,\tau \geq 10$, and reasonably good in the preasymptotic region, $1 < (1-g)\,\tau < 10$, with correction terms in Eqs. (12a,b) and (13).

The MC computations were performed for a diffuse boundary-source rather than a normally incident collimated source that would better model a laser beam. Also, the phase function used in the simulations was Henyey and Greenstein's (1941) smooth model rather than Mie calculations with a strong forward peak. However, these caveats only affect low orders-of-scattering, which dominate the signal only if the clouds have a small optical depth; such clouds are readily probed by on-beam lidar methods anyway. Furthermore, the validity of the analytical theory can be extended to account for these directional effects by using the δ-Eddington reformulation of the diffusion approximation (Joseph et al., 1976).

2.4. Implications for off-beam lidar observations

From Eq. (11), the rms "spot-radius" $\langle \rho^2 \rangle_{\mathrm{R}}^{1/2}$ is found to be ≈ 0.3 km for the mean optical depth ($\tau \approx 13$) and physical thickness ($H \approx 0.3$ km) of marine stratocumulus (Sc), as observed by Cahalan and Snider (1989), and using the canonical $g = 0.85$ for warm clouds. This rms spot-size is a key quantity in the a priori signal-to-background ratio estimations by Davis and Cahalan (1998). Returning to the ground-based observation geometry in Fig. 1, $\langle \rho^2 \rangle_{\mathrm{R}}^{1/2} \approx 0.3$ km implies that we need a FOV of about 1 rad to capture about 2 rms distances if the cloud is at a range $d_{\mathrm{obs}} \approx 1$ km. A couple of rms spot-radii, i.e., 0.5 km or so, is also the inherent resolution of a retrieval based on off-beam lidar observations, even if they are done continuously in time.

Optical depth τ is in fact highly variable at the sub-kilometer scales of interest here: its range is from less than 5 to almost 100. This optical depth range alone leads to an albedo R between 0.9 and 0.3 in Eq. (8), which is another important factor in signal estimation. High R values imply that after the laser hits cloud base, plenty of light is eventually returned towards the ground.

The range of variation for H corresponding to that in τ, as given partially by the Pawlowska et al. (2000) $\tau \propto H^{5/3}$ relation, is 0.2–0.6 km. This relation applies however only to the adiabatic "cores" of Sc, hence to the relatively high τ values (> 10) at the local maxima in the optical depth (or solar reflectance) fields; at the smaller but still highly variable τ's observed more frequently in sub-adiabatic regions, this τ–H coupling breaks down, with H varying spatially more slowly than τ in Sc.

For temporal quantities, we find $\langle \lambda \rangle_{\mathrm{R}}$ to be somewhat larger than H, in the range 0.4–0.8 km, while the ratio $\langle \lambda^2 \rangle_{\mathrm{R}}^{1/2} / \langle \lambda \rangle_{\mathrm{R}}$ falls between 1.5 and 2. These values were also used in the design phase of our instrument to set pulse-length requirements and time-binning strategies. Note that the precise choice for χ, always coupled to g and τ in our correction formulas Eqs. (12a,b) and (13), has a minor effect on these λ statistics in the intermediate diffusive transport regime where correction terms are not negligible.

2.5. Summary of theoretical results

The key result of the analysis above is that by combining the temporal and spatial information from off-beam lidar—the mean pathlength from the temporal Green func-

tion, Eq. (9), and the mean-square horizontal displacement from the spatial Green function, Eq. (11) — both the cloud thickness H and optical depth τ can be determined. A time-only retrieval of H and τ can, in principle, be obtained using the first two moments of the temporal Green function. As we shall see in Section 5, however, the time-only retrieval is subject to much greater uncertainties than the full space–time retrieval.

In dealing with the spatial information, the analysis described here has dealt exclusively with the radial displacement. As we have seen, considerable information can be obtained from such an azimuthally averaged approach. However, the most informative realization of off-beam lidar would be one in which not only the radial and temporal distributions of the returning light are recorded, but its azimuthal dependence as well. This amounts to full time-resolved 2D imaging of the scattered radiation, in essence, a high-speed "movie" of the light propagation. With such a system, not only are quasi-uniform cloud fields amenable to azimuthally averaged analysis, but complex scattering mechanisms (scattering between clouds, etc.) in highly non-uniform clouds and broken cloud decks may also be observed and interpreted.

3. Description of the Wide-Angle Imaging Lidar instrument

The basic idea of WAIL is to send a short-pulse, narrow-beam laser into a cloud, and record, as a function of both space and time, the intensity of the returning light over a wide field-of-view. In essence, one wants to take a "movie" of the propagation of the multiply scattered light. The realization of such a fully imaging WAIL instrument relies on unique imaging detector technology developed at Los Alamos National Laboratory, the Micro-channel Plate/Crossed Delay Line (MCP/CDL) detector, coupled with high-speed pulse absolute timing electronics (Priedhorsky et al., 1996). The MCP/CDL technology features photon-counting sensitivity, a large spatial format (4 cm diameter active area, effectively up to $\approx 1500^2$ pixels), and ultra-high time resolution (100 ps). It consists of the MCP/CDL detector—a photo-cathode coated vacuum tube, intensified by micro-channel plates, read out by a crossed delay line anode — together with fast pulse-timing electronics. Each photo-electron is intensified by a factor of 10^7, with positional information preserved, by the MCP. The electron cloud is collected by helically wound delay lines, producing in each line two counter-propagating current pulses which emerge from the ends. By measuring the arrival times of the pulses at the ends of the delay lines, the position of the original photon event is determined; with two orthogonal delay lines, both the x- and y-coordinates are determined.

This unique strategy for extracting spatial information distinguishes the MCP/CDL from other sensitive imagers such as gated/intensified CCDs in that it is intrinsically very fast, with photon arrival time automatically known to within 100 ps as a by-product of the imaging scheme. As an early test, we exploited this extremely high time resolution (100 ps corresponds to a pathlength of only 3 cm) to perform laboratory-scale simulations of off-beam lidar, where the "cloud" was a sizeable aquarium filled with a scattering liquid

suspension (Davis et al., 1998). One final thing to note about the idiosyncracies of this detector is that it is not only capable of performing at very low light levels, but actually requires them: too high a count rate ($>5\times10^6$/s over the entire detector) confuses the timing-based imaging scheme.

These strengths and limitations drive the choice of laser for the imaging lidar system. The count rate limit demands a high repetition rate and averaging over many pulses. A repetition rate around 5–15 kHz is ideal, permitting maximal pulse averaging while avoiding the return from one pulse overlapping with the next. The MCP's spectral response makes a 532 nm frequency-doubled Nd:YAG laser a good choice. Our current laser produces 0.2 to 0.5 mJ/pulse, at a variable rep rate (12 kHz is typical in our experiments), with pulse widths ranging from 30 to 50 ns depending on operating conditions. The laser is triggered by a master clock, which also provides the timing reference for the detector system electronics.

Our current nighttime WAIL implementation uses a standard medium-format camera lens with a 35-mm focal length to feed the detector, thus obtaining the full angle FOV of 60° prescribed in Section 2. One challenge in designing an imaging lidar system for clouds is the large dynamic range, several orders of magnitude, between the initial return (the traditional on-beam lidar signal) and the multiply scattered returns from locations at very large displacements from the beam. The faint large-displacement returns require a band-pass filter, ≈ 10 nm wide for nighttime work, to reject as much background light as possible. Table 1 summarizes the parameters of the instrument.

The use of interference filters presents an apparent problem, given the wide FOV, since, as is well known, the band center for standard interference filters varies strongly with angle of incidence. Over the 30° half-angle range of our system, the passband center wavelength shifts nearly 15 nm to shorter wavelengths as one moves from the center to the edge of the field. This angular sensitivity, however, can be put to use to partially cancel the strong center-to-edge gradient intrinsic to cloud returns but challenging to any detector system, particularly to our MCP/CDL. If, instead of a filter centered (at normal incidence) at the laser wavelength, one chooses a somewhat longer nominal filter wavelength, light at large angles of incidence (i.e., coming from the edge of the FOV) will be near the angle-shifted center of the filter passband, while light near normal incidence (i.e., coming from the bright central spot) will be in the wings of the filter passband and be strongly

Table 1
Instrumental characteristics of LANL's Wide-Angle Imaging Lidar System. Notice the unusually wide FOV and the correspondingly small focal length. Furthermore, given the $f/\#$ range, apertures were miniscule by on-beam lidar standards, between 1 cm and 1.6 mm only

Transmitter		Receiver	
Pulse energy	0.2–0.5 mJ	Focal length	35 mm
Repetition rate	12 kHz	$f/\#$	3.5–22
Pulse width	30–50 ns	FOV (Ø) at focal plane	60° (4 cm)
Wavelength	532 nm	Detector-type	MCP/CDL
Laser type	Nd:YAG	Effective angular pixels	$\approx 1500^2$
Cooling	water	Time bin width	40 ns
Manufacturers	laser: Cutting-Edge Opticronics	Optics: Pentax, Detector: LANL	

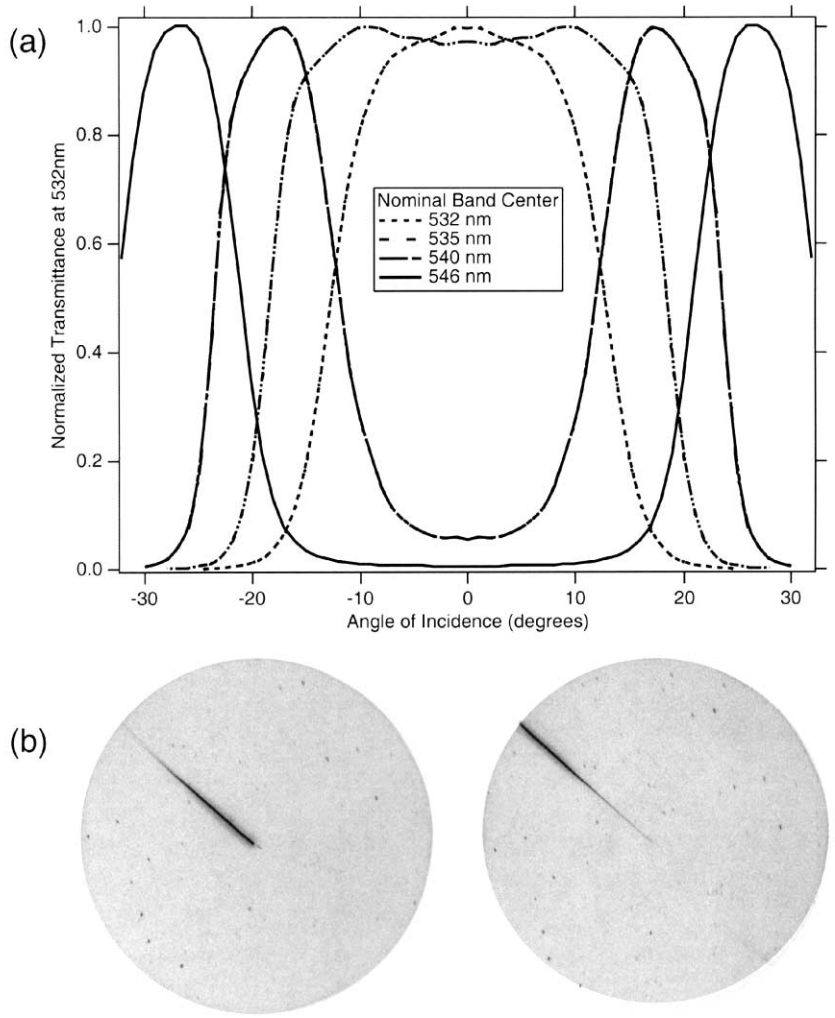

Fig. 3. Bandpass interference filters as angular response filters. (a) Transmission vs. angle of incidence at 532 nm for our 10-nm bandpass interference filter collection. (b) Time-integrated WAIL images illustrating the angular selectivity using (broadband) star light and aerosol-scattered (532 nm) laser light for the filters centered nominally at 532 (left) and 546 nm (right); the laser beam, in upper right hand corner, is respectively transmitted and suppressed in the center, vice-versa in the outer region. Black spots are stars; Ursa Major is at lower left. Note that WAIL is in an effectively bistatic configuration for the near field scattering.

attenuated. Fig. 3a shows the empirical transmission function of our filter collection with respect to incidence angle out to 30° for 532-nm light. Fig. 3b shows WAIL images illustrating the angular response of two filters using broadband starlight and the 532-nm laser beam.

4. Off-beam cloud lidar observations from the ground

4.1. Sample dataset

Now we shall examine an example of actual WAIL data, collected July 8, 1999, between 00:30 and 01:00 MST at LANL's Fenton Hill Observatory (35°52′ 45″N, 106°40′ 37″W). Fig. 4 shows these nighttime results for a multi-layer cloud deck, probed with two different filters on the detector, one (nominal band center at 540 nm) which strongly suppresses the center spot, and the other (nominal band center at 536 nm) providing a more uniform response across the field. In each case, the spatially integrated return as a function of time (i.e. the temporal Green function) is plotted, along with representative frames of the spatial WAIL "movie", each frame showing the full 60° FOV.

At early times, we see the near-field aerosol scattering. This eventually is followed by multiple cloud-base impacts, and finally by a strong spreading due to multiple scattering in the highest/densest layer. Due to the existence of a maximum allowable throughput for the focal-plane detector, the signal originating from the impact point and nearby is saturated, especially when the 532 nm (center-field) filter was used. However, we have minimized the impact of this loss of signal at small (include) pathlength λ and small horizontal displacement ρ by computing the space–time moments of interest further on using only the intermediate 540-nm filter. The effective truncation of long pathlengths and displacements compensates for the residual saturation at small times and angles. In an ideal situation, we would merge the signals from the more extreme (532 or 535 and 546 nm) filters in Fig. 4a,b before computing the moments in Eqs. (4)–(6).

For QuickTime™ movie versions of these and other datasets, see http://nis-www.lanl.gov/~love/clouds.html.

4.2. Cloud property retrievals

In Fig. 5, the analysis of Section 2 is applied to the WAIL data shown in Fig. 4. Two methods for extracting physical cloud thickness H and optical depth τ are shown, one in which we make use of both the spatial and temporal information contained in the WAIL data (the most accurate method), and a second method which uses only the temporal information. This latter, time-only analysis is useful in that it can be applied to simpler non-imaging off-beam lidar systems. Reassuringly, the cloud parameters obtained from the two methods are consistent with each other and appear reasonable for the altostratus layer that was visually observed during the measurement. To achieve this congruence of the methods it is important to account for the internal stratification of the cloud layer. Indeed, we have plotted the results of numerical simulations similar to those described in Section 2.3 but with a collimated beam normally incident onto (1) uniform cloud models and (2) vertically stratified cloud models. Only the latter results explain the data in terms of the $\langle\lambda^2\rangle_R^{1/2}/\langle\lambda\rangle_R$ ratio used below. We assumed a linear increase of extinction from zero at cloud base to $2\tau/H$ at cloud top. This is a worse case since Brenguier (1991) parameterization for adiabatic cores calls for a linear increase in LWC which, in turn, leads to a 2/3 power law in extinction (Pelon et al., 2000). The two versions of the two-parameter retrieval procedure are as follows.

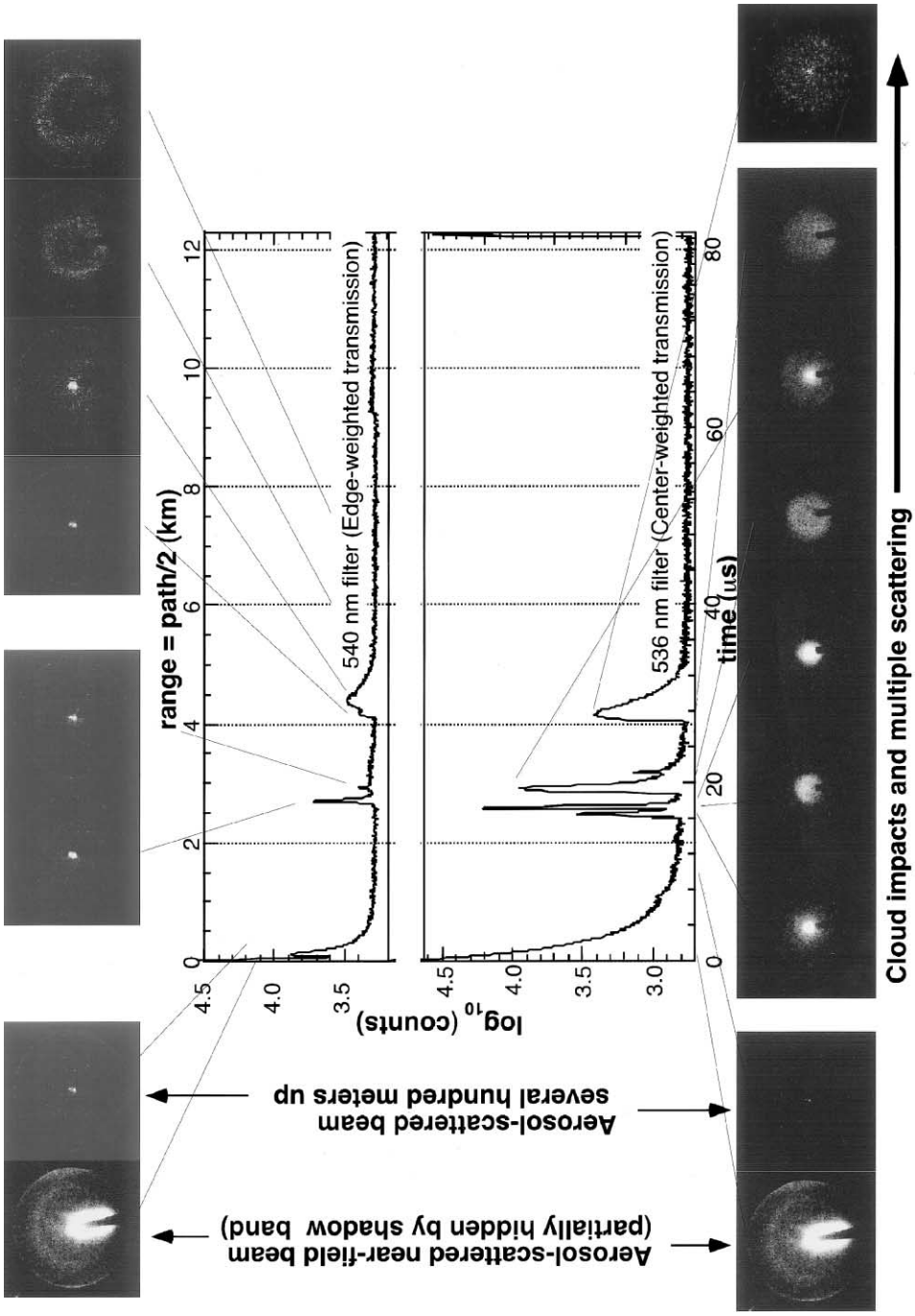
Aerosol-scattered near-field beam
(partially hidden by shadow band)
Aerosol-scattered beam
several hundred meters up
range = path/2 (km)
log10 (counts)
540 nm filter (Edge-weighted transmission)
536 nm filter (Center-weighted transmission)
time (μs)
Cloud impacts and multiple scattering

In both cases, the lower curve determines the optical depth τ. However, we immediately notice the large range of possible values for τ in the time only scheme of Fig. 5a based on the ratio of ratios $\langle\lambda^2\rangle_R^{1/2}/\langle\lambda\rangle_R$ from Eqs. (4) and (5) which yields 1.16: τ can be anywhere from 2 to 10 (even 1 to 20 or broader, given some measurement error). The cloud height information in Fig. 5 (this is an altostratus) argues for the lower end of the range in τ but we proceed without using this. From the upper curve, the cloud thickness can be determined, given the mean pathlength $<\lambda>_R \approx 1.37$ km. The inferred value of H is, fortunately, not very sensitive to τ and we find H between 0.48 (possibly a little less, given some measurement error) to 0.56 km. This is reasonable for the nocturnal altostratus layer present in Fig. 4.

For the combined space-time theme, substituting the response curves in Fig. 5b yields similar results, starting with $\langle\rho^2\rangle_R^{1/2}/\langle\lambda\rangle_R$ from Eqs. (4) and (6), which yields 0.76, but there is less uncertainty in τ and H. The inferred value for τ of about 3 is quite reasonable for altostratus and the associated H is in the middle of the previously obtained range, around 0.52 km. The time-only and space–time methods thus yield compatible results.

Consider now the well-known relation between optical depth and liquid water path (LWP), the vertical integral of LWC: $\tau = (3/2)\mathrm{LWP}/\rho_w r_e$ (Stephens, 1978), where ρ_w is the density of liquid water (i.e., 10^6 g/m^3). Thus, with an additional assumption on the effective droplet radius r_e, the volume-averaged LWC can be estimated using an optical WAIL measurement alone:

$$\overline{\mathrm{LWC}} = \mathrm{LWP}/H = (2/3)\rho_w(r_e/H)\tau; \tag{14}$$

no radiosondes, nor microwave instruments are required. For instance, taking $r_e \approx 10$ μm for simplicity, we find $\overline{\mathrm{LWC}} \approx 0.036$ g/m^3 in our altostratus case.

Finally, the "natural" horizontal resolution we can assign to our (τ, H) estimates, and hence to LWC in Eq. (14), is $\approx 2\langle\rho^2\rangle_R^{1/2}$. For our case study, we obtain ≈ 1 km, which is similar to those state-of-the-art meteorological satellites capable of synoptic coverage.

4.3. Discussion

If we limit ourselves to the time-only retrieval scheme (as was the case in the space-based LITE experiment, which inadvertently implemented off-beam lidar due to the wide FOV used — see Winker, 1997; Miller and Stephens, 1999; Davis et al., in press), the

Fig. 4. Nighttime WAIL results. Shown here are the spatially integrated total return as a function of time (graphs) and a sequence of selected frames from the corresponding WAIL "movies", which show the spatial distribution of the returning light as a function of time. The full-angle FOV is approximately 60°. Two data sets for essentially the same cloud deck are shown, taken a few minutes apart. These were obtained with two different filters on the optics, one which emphasizes the large-angle returns (top) and the other emphasizing the center region (bottom). Narrow bandpass interference filters are generally used to reject background light, but also affect the spatial response of the system (see text and Fig. 3 for more details). Each sequence begins with the Rayleigh/aerosol-scattered beam as it leaves the laser (located off the bottom right side of the FOV); a shadow band blocks the brightest portion of this early return. For these early times, the system is effectively bistatic. Subsequent frames show the aerosol-scattered pulse several hundred meters up, the initial impact on the cloud deck, and subsequent spreading due to multiple scattering.

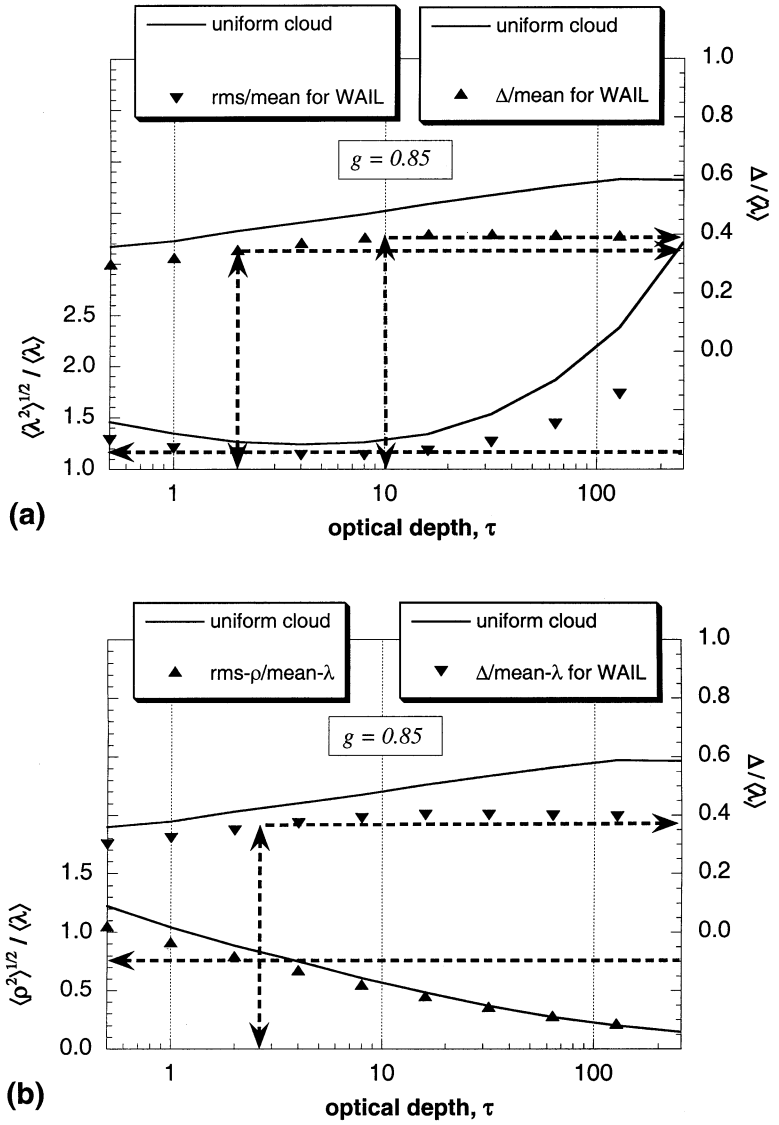

Fig. 5. Retrieval of cloud properties from WAIL data. (a) Time-only scheme. (b) Combined space–time scheme. In each case, the lower curve shows the calculated ratio of a second-order moment (rms pathlength for the time-only scheme; rms spot radius for the space–time scheme) to the first-order moment of the pathlength distribution. The ratio is plotted as a function of optical depth for a uniform cloud (line) and for a more realistic stratified cloud (symbols) for the ground-based geometry. The upper curves are calculated ratios of the cloud thickness to mean pathlength. Retrieval of cloud properties proceeds by noting the moment ratio from measured WAIL data (see main text), indicated here by the lower dashed horizontal line. The intersection of this line with the lower curve defines the optical depth (with considerable uncertainty in the time-only scheme). A vertical line drawn from the intersection to the upper curve yields the cloud physical thickness. In this case the mean pathlength was found to be ≈ 1.37 km, yielding a physical cloud thickness of approximately 0.5 km.

large ambiguity in optical depth τ could be removed be using an empirical estimate of R in Eq. (2). Curiously enough, with our WAIL system this cloud albedo measurement would be from below. However, as is well known to the satellite remote-sensing community, R determination requires proper calibration of the system. If we go to this trouble, we would hope to recover an extra piece of information about the cloud, such as its internal variability at unresolved scales. This of course calls for a refined theory that would account for horizontal as well as vertical variability. This is probably best done with a variability model with a single parameter such as a Gamma distribution for optical depths; Barker (1996) advantageously used this model in his enhanced radiation scheme for numerical climate models. A similar enhancement of off-beam lidar retrieval schemes restores, in a statistical sense, the capability of on-beam systems to resolve internal cloud structure.

One can also remark that $\tau \approx 3$ is not inaccessible with a powerful enough on-beam system as long as the appropriate corrections are made for multiple small-angle scatterings along both paths (Platt, 1973). It is also true a priori that off-beam lidar becomes more accurate as τ becomes ever larger, thus complementing perfectly on-beam techniques. However, the saturation observed in our present detector increases with overall cloud reflectivity R, hence τ. So the case-study presented here is a workable compromise while we continue to explore better solutions to the saturation problem, including stronger suppression of the central region using an occulting disk, and perhaps a new detector with different space/time-resolution tradeoffs.

For dense clouds that will extinguish on-beam backscatter lidar signals, active microwave (mm-radar) devices can be used to infer LWC in comparable detail: a number of vertical bins, typically several per cloud layer, and with a horizontal resolution that depends on that observation strategy, but is typically a few hundred meters. So, in principle, these complementary instruments appear to yield more information than WAIL on cloud structure. However, Clothiaux et al. (1995) detailed comparisons of mm-radar datastreams with counterparts from collocated (on-beam) lidar and other instruments underscore several problems in the conversion of radar reflectivities to the optical (shortwave) quantities required to pursue, say, climate studies. In contrast, off-beam lidar operates at wavelengths that are fully representative of solar radiative transfer. Even assuming a tenuous enough cloud to still detect usual on-beam lidar signal and sufficient skill to correct it for the multiple forward scattering, the inversion of this signal (Klett, 1981) is highly sensitive to the choice of backscatter ratio; this, in turn, depends on the phase function value for 180° scattering, which is a well-documented challenge to Mie theory. Being based on scattering through all possible angles, off-beam lidar does not have such sensitivities and the resulting spatial resolution is adequate for many applications.

5. Summary and outlook

We have described a significant new extension of lidar technology, wide-angle imaging lidar, and have shown how it can be used to determine cloud properties never before accessible to a purely optical measurement. We have shown that WAIL, and more

generally off-beam lidar, can be used to measure both the physical thickness of a stratiform cloud and its optical depth at scales of about 0.5 km. In earlier work we demonstrated (Davis, 1999; Davis et al., in press) that similar information can be extracted from a non-imaging spaceborne lidar system with a wide-enough FOV, e.g. the shuttle-based LITE mission. Within instrumental and modeling error, both the "time-only" method used for LITE data and the "space–time" method presented here yield mutually consistent results. However, the combined space–time scheme, which calls for a device with imaging (or at least radial profiling) capability, provides a much less ambiguous measure of optical depth.

The transmitter and optics we use are standard commercially available products, while the imaging detector is a custom LANL design described in some detail by Priedhorsky et al. (1996). The detector has the advantages of high angular and temporal resolutions as well as extreme sensitivity. Its major disadvantage is the relatively low maximum allowable count rate, which necessitates co-adding many laser pulses in order to achieve good statistics on the scattered returns. The strong spatial gradient of the cloud returns, with most of the light coming from the nearly on-beam area, exacerbates this problem. Our current solution to this problem is to use interference filters to make the intensity distribution at the focal plane as uniform as possible. Residual saturation still occurs and we have accounted for this in our analysis of the data. In the near future, we will explore alternative solutions for this problem, including the use of an occulting disk to completely mask the central region while obtaining large-angle data, and possibly the use of a different type of detector.

While WAIL provides a very exhaustive data set, extrapolation to a space-based system presents many technical challenges. Therefore, parallel to the WAIL project, a collaborative work currently underway at NASA Goddard Space Flight Center is focused on a scheme using more conventional detectors fed by an optical train that is customized for airborne observation. In this design, the radial information is preserved but averaged azimuthally in the hardware, which incorporates fiber-optic bundles to route the light from pre-defined radial zones to several separate high-sensitivity photo-detectors. Meanwhile, at LANL we are developing daylight capability for WAIL by means of ultra-narrow magneto-optic filters coincident with strong solar Fraunhofer absorption lines. This strategy requires a new transmitter tuned to the highly selective wavelength.

There is also a need for improved theory in off-beam lidar. In particular, the analytical approach grounded in photon diffusion theory can be extended at once to lesser optical depths and illumination by a collimated beam by using δ-rescaling of the optical properties in a 3D setting. Also, the numerical modeling can be enhanced by accounting for horizontal as well as vertical structure in the cloud; Davis et al. (1997b) show some early Monte Carlo results on horizontal variability effects. In this context, it is desirable to have codes to solve both the radiative transfer problem (using, e.g., Monte Carlo) and the diffusion problem (using, e.g., finite elements).

Regardless of which instrumental design gains the widest acceptance, which modeling approach prevails, and which retrieval scheme proves most robust, it is clear that off-beam lidar can provide a valuable and cost-effective tool for remote probing of cloud properties.

Acknowledgements

This work was supported financially by the Laboratory Director's Research and Development (LDRD) program, under an "Exploratory Research" project. We thank A. Bird, D. Casperson and R.C. Smith for detector expertise and assistance with the data collection. We also thank R. Cahalan, A. Marshak, M. McGill, W. Priedhorsky, J. Spinhirne, J. Weinman, D. Winker, W. Wiscombe, and E. Zege for many fruitful discussions that helped shape this new approach to cloud lidar probing and its implementation in WAIL.

References

Barker, H.W., 1996. A parameterization for computing grid-averaged solar fluxes for inhomogeneous marine boundary layer clouds: Part 1. Methodology and homogeneous biases. J. Atmos. Sci. 53, 2289–2303.

Brenguier, J.-L., 1991. Parameterization of the condensation process: a theoretical approach. J. Atmos. Sci. 48, 264–282.

Bissonnette, L.R., 1995. Multiple scatttering of narrow light beams in aerosols. Appl. Phys. B 60, 315–323.

Cahalan, R.F., Snider, J.B., 1989. Marine stratocumulus structure during FIRE. Remote Sens. Environ. 28, 95–107.

Case, K.M., Zweifel, P.F., 1967. Linear Transport Theory. Addison-Wesley Publ., Reading, MA.

Clothiaux, E.E., Miller, M.A., Albrecht, B.A., Ackerman, T.P., Verlinde, J., Babb, D.M., Peters, R.M., Syrett, W.J., 1995. An evaluation of a 94-GHz radar for remote sensing of cloud properties. J. Atmos. Oceanic Technol. 12, 201–229.

Davis, A.B., 1999. Physical thickness and optical depth of stratocumulus from space-borne lidar. A Moment-Based Diffusion Method. Technical Digest of OSA Topical Meeting of "Optical Remote Sensing on the Atmosphere", June 21–25, 1999, Santa Barbara, CA, Optical Society of America, Washington, DC, pp. 66–68.

Davis, A.B., Cahalan, R.F., 1998. Off-beam (multiply scattered) lidar returns from status: 1. Cloud-information content and sensitivity to noise. In: Singh, U., Ismail, S., Schwemmer, G. (Eds.), 19th International Laser Radar Conference Proceedings, July 6–10, 1998. NASA Center for Aero-Space Information (CASI), Annapolis, MD, pp. 91–94.

Davis, A.B., Marshak, A., 2001. Space–time characteristics of light transmitted by dense clouds. J. Atmos. Sci. (submitted for publication).

Davis, A.B., Winker, D.M., Marshak, A., Spinhirne, J.D., Cahalan, R.F., Love, S.P., Melfi, S.H., Wiscombe, W.J., 1997a. Retrieval of physical and optical cloud thicknesses from space-borne and wide-angle lidar. In: Ansmann, A., Neuber, R., Rairoux, P., Wadinger, U. (Eds.), Advances in Atmospheric Remote Sensing with Lidar. Springer-Verlag, Berlin, Germany, pp. 193–196.

Davis, A.B., Marshak, A., Cahalan, R.F., Wiscombe, W.J., 1997b. The LANDSAT scale-break in stratocumulus as a three-dimensional radiative transfer effect, implications for cloud remote sensing. J. Atmos. Sci. 54, 241–260.

Davis, A.B., Ho, C., Love, S.P., 1998. Off-beam (multiply-scattered) lidar returns from stratus: 2. Space–time measurements in a laboratory simulation. In: Singh, U., Ismail, S., Schwemmer, G. (Eds.), 19th International Laser Radar Conference Proceedings, July 6–10, 1998. NASA Center for Aero-Space Information (CASI), Annapolis, MD, pp. 55–58.

Davis, A.B., Cahalan, R.F., Spinhirne, J.D., McGill, M.J., Love, S.P., 1999. Off-beam lidar: an emerging technique in cloud remote sensing based on radiative Green-function theory in the diffusion domain. Phys. Chem. Earth B 24, 757–765.

Davis, A.B., Winker, D.M., Vaughan, M.A., 2001. First retrieval of boundary-layer cloud properties from off-beam / multiple-scattering lidar data collected in space. In: Dabas, A., Loth, C., Pelon, J. (Eds.), Laser Remote Sensing of the Atmosphere: Selected Papers from the 20th International Laser Radar Conference. Editions de l'École Polytechnique, Palaiseau, France, pp. 35–38.

Deirmendjian, D., 1969. Electromagnetic Scattering on Spherical Polydispersions. Elsevier, New York, NY.
Eddington, A.S., 1916. On the radiative equilibrium of stars. Mon. Not. R. Astron. Soc. 77, 16–35.
Henyey, L.C., Greenstein, J.L., 1941. Diffuse radiation in the galaxy. Astrophys. J. 93, 70–83.
Joseph, J.H., Wiscombe, W.J., Weinman, J.A., 1976. The delta-Eddington approximation for radiative flux transfer. J. Atmos. Sci. 33, 2452–2459.
Klett, J.D., 1981. Stable analytical inversion solution for processing lidar returns. Appl. Opt. 20, 211–220.
Mandelbrot, B.B., 1982. The Fractal Geometry of Nature. W.H. Freeman, San Francisco, CA.
Miller, S.D., Stephens, G.L., 1999. Multiple scattering effects in the lidar pulse stretching problem. J. Geophys. Res. 104, 22205–22219.
Pawlowska, H., Brenguier, J.-L., Fouquart, Y., Armbruster, W., Bakan, S., Descloitres, J., Fischer, J., Flamant, C., Failloux, A., Gayet, J.-F., Gosh, S., Jonas, P., Parol, F., Pelon, J., Schüller, L., 2000. Microphysical and radiative properties of stratocumulus clouds: the EUCREX mission 206 case study. Atmos. Res. 55, 85–102.
Pelon, J., Flamant, C., Trouillet, V., Flamant, P.H., 2000. Optical and microphysical parameters of dense stratocumulus clouds during mission 206 of EUCREX'94 as retrieved from measurements with the airborne lidar LEANDRE 1. Atmos. Res. 55, 47–64.
Platt, C.M.R., 1973. Lidar and radiometric observations of cirrus clouds. J. Atmos. Sci. 30, 1191–1204.
Priedhorsky, W.C., Smith, R.C., Ho, C., 1996. Laser ranging and mapping with a photon-counting detector. Appl. Opt. 35, 441–452.
Sassen, K., 1994. Advances in polarization diversity lidar for cloud remote sensing. Proc. IEEE 82, 1907–1914.
Savigny, C., Funk, O., Platt, U., Pfeilsticker, K., 1999. Radiative smoothing in zenith-scattered sky light transmitted through clouds to the ground. Geophys. Res. Lett. 26, 2949–2952.
Stephens, G.L., 1978. Radiation profile in extended water clouds: Part 1. Theory. J. Atmos. Sci. 35, 2111–2122.
Veitel, H., Funk, O., Kruz, C., Platt, U., Pfeilsticker, K., 1998. Geometrical pathlength probability density functions of the skylight transmitted by mid-lattitude cloudy skies. Geophys. Res. Lett. 25, 3355–3358.
Winker, D.M., 1997. Simulation and modeling of the multiple scattering effects observed in LITE data. In: Ansmann, A., Neuber, R., Rairoux, P., Wadinger, U. (Eds.), Advances in Atmospheric Remote Sensing with Lidar. Springer-Verlag, Berlin, Germany, pp. 185–188.